PHYSICAL REVIEW C VOLUME 58, NUMBER 4 OCTOBER 1998

Observation of kaonic hydrogen atom x rays

T. M. Ito,* R. S. Hayano, S. N. Nakamura,† and T. P. Terada
Department of Physics, University of Tokyo, 7-3-1 Hongo, Bunkyo, Tokyo 113-0033, Japan

M. Iwasaki
Department of Physics, Tokyo Institute of Technology, 2-12-1 Ookayama, Meguro, Tokyo 152-8551, Japan

D. R. Gill, L. Lee,‡ A. Olin, M. Salomon, and S. Yen
TRIUMF, 4004 Wesbrook Mall, Vancouver, British Columbia, Canada V6T 2A3

K. Bartlett,§ G. A. Beer, G. Mason, and G. Trayling
Department of Physics and Astronomy, University of Victoria, Box 3055, Victoria, British Columbia, Canada V8W 3P6

H. Outa‖
Institute for Nuclear Study, University of Tokyo, 3-2-1 Midori, Tanashi, Tokyo 188-0002, Japan

T. Taniguchi and Y. Yamashita¶
KEK, 1-1 Oho, Tsukuba, Ibaraki 305-0801, Japan

R. Seki**
W. K. Kellogg Radiation Laboratory, California Institute of Technology, Pasadena, California 91125

(Received 3 June 1998)

We have measured the *K*-series x rays from kaonic hydrogen atoms and have succeeded for the first time in observing a distinct $K\alpha$ peak. The *L* x-ray peak has also been observed. The strong-interaction shift and width of the kaonic hydrogen atom $1s$ state were determined from the transition energy and the line width of the $K\alpha$ x rays. The sign of the strong-interaction shift was confirmed to be repulsive, with the results $\Delta E_{1s} = -323 \pm 63$ (statistical) ± 11 (systematic) eV and $\Gamma_{1s} = 407 \pm 208 \pm 100$ eV. The measured shift and width of the $1s$ state are consistent with those expected from other low energy $\overline{K}N$ data, and thus the long-standing kaonic hydrogen puzzle is resolved. The $K\alpha$ x-ray yield per stopped kaon was estimated to be $1.5 \pm 0.5\%$ at a hydrogen target density of $10\rho_{\text{STP}}$. [S0556-2813(98)05710-0]

PACS number(s): 13.75.Jz, 25.80.Nv, 29.30.Kv, 36.10.Gv

I. INTRODUCTION

The kaonic hydrogen atom, a system composed of a proton and a negatively charged kaon bound by the Coulomb force, serves as a unique tool to probe the $\overline{K}N$ interaction at the threshold energy. Its energy levels are shifted from their pure electromagnetic values and have a finite absorption width due to the strong interaction between the kaon and the proton. The shift and width are appreciable only in the $1s$ state and are negligible in other states in comparison. It is thus expected that the shift and width of the $1s$ state can be determined by measuring the energy of the *K*-series x rays. The $1s$ state shift and width can be related to the real and imaginary parts of the K^-p scattering length a_{K^-p} by the Deser-Trueman formula [1]

$$\Delta E_{1s} + \frac{i}{2}\Gamma_{1s} = 2\alpha^3\mu^2 a_{K^-p} = 412 \text{ eV fm}^{-1}\ a_{K^-p}, \quad (1)$$

where $\Delta E_{1s} = E^{\text{expt}}_{2p\to 1s} - E^{\text{E.M.}}_{2p\to 1s}$, μ is the reduced mass of the K^-p system, and α is the fine structure constant. The K^-p *s*-wave scattering length a_{K^-p} is related to the $\overline{K}N$ scattering lengths in the $I=0$ and $I=1$ channels through $a_{K^-p} = \frac{1}{2}(a_0 + a_1)$. Also, the $2p$ state width can be determined by comparing the total intensity of the *L* x rays to the $K\alpha$ x rays. The width is related to the imaginary part of the K^-p *p*-wave scattering volume in a similar fashion to Eq. (1).

The study of the $\overline{K}N$ interaction has vital importance in understanding the strong interaction in the low-energy re-

---

*Present address: W. K. Kellogg Radiation Laboratory, California Institute of Technology, Pasadena, CA 91125.

†Present address: Muon Science Laboratory, The Institute of Physical and Chemical Research (RIKEN), 2-1 Hirosawa, Wako, Saitama 351-0198, Japan.

‡Present address: Department of Physics, University of Manitoba, Winnipeg, MB, Canada R3T 2N2.

§Present address: Ocean Acoustics Group, Institute of Ocean Sciences, 9860 West Saanich Road, Box 6000, Sidney, BC, Canada V8L 4B2.

‖Present address: KEK, 1-1 Oho, Tsukuba, Ibaraki 305, Japan.

¶Present address: Tokyo Metropolitan Adachi Nichi Senior High School, 5-7-1 Kouhoku, Adachi, Tokyo 123-0872, Japan.

**Also at: Department of Physics and Astrophysics, California State University, Northridge, CA 91330.

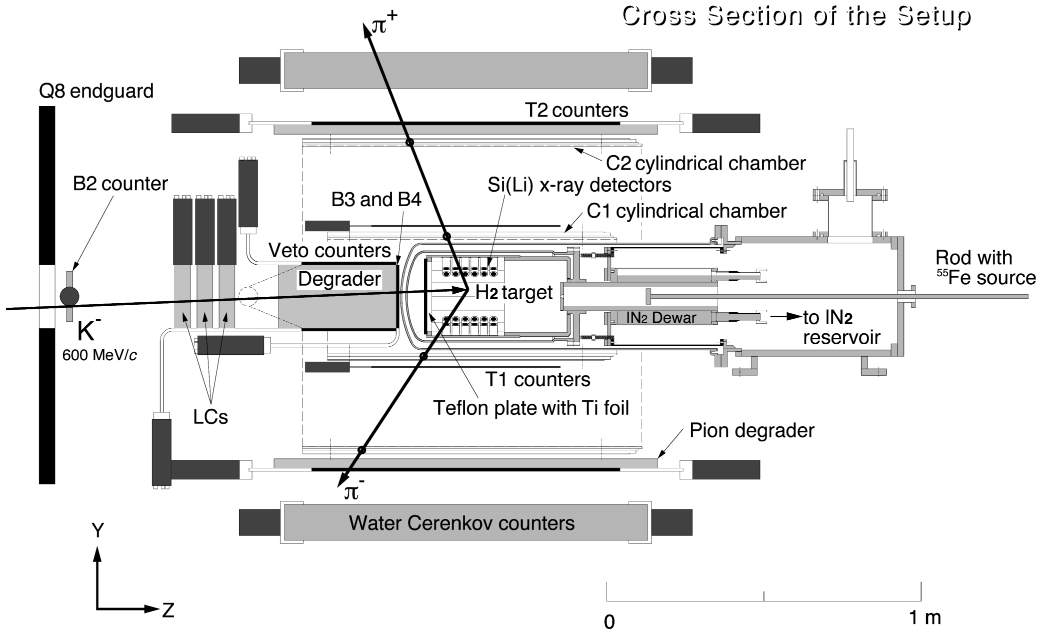

FIG. 1. Experimental apparatus (cross section). Negative kaons of 600 MeV/c were slowed down in the carbon degrader and brought to rest in the hydrogen gas target, forming kaonic hydrogen atoms. The timing of the incoming beam was determined by the B2 counter. Three Lucite Čerenkov counters served for K/π separation. X rays from kaonic hydrogen atoms were detected with the Si(Li) x-ray detectors placed in the hydrogen volume. The two layers of scintillation counter arrays (T1 and T2), the two cylindrical MWPCs (C1 and C2), and the water Čerenkov counter array surrounding the target served to detect two charged pions from K^-p absorption to select appropriate events.

gion. A resonant state $\Lambda(1405)$ couples to the $\bar{K}N$ system just below the $\bar{K}N$ threshold in the $I=0$ channel. The $\Lambda(1405)$ is one of the most poorly understood objects among low-mass baryons. The dispute about its structure, whether it is a $\bar{K}N$ bound state [2–4] or a three-quark state [5,6], is still unresolved. Since the $\Lambda(1405)$ resonance dominates the $I=0$ $\bar{K}N$ amplitude near threshold, it is expected that the structure of the $\Lambda(1405)$ can be investigated through study of the low-energy $\bar{K}N$ interaction, in particular, through measurement of kaonic hydrogen atom x rays. More importantly, systematic studies of the low-energy KN and $\bar{K}N$ interactions will allow a more reliable determination of the KN Σ term (Σ_{KN}), which is related to the strangeness content of the proton [7].

At present experimental data are available for (a) K^-p elastic and inelastic cross sections, (b) branching ratios for the K^- absorption at rest in hydrogen, (c) $\Sigma\pi$ invariant mass distribution below the $\bar{K}N$ threshold [showing the $\Lambda(1405)$ resonance bump], and (d) three measurements of kaonic hydrogen x rays [8–10]. The results of the previous studies of the low-energy $\bar{K}N$ interaction are quite puzzling. Conventional analyses of data for (a)–(c) find that $\mathrm{Re}\,a_{K^-p}<0$. For example, Martin [11] obtained $a_0=-1.70+i0.68$ fm and $a_1=0.37+i0.60$ fm. From Eq. (1), if $\mathrm{Re}\,a_{K^-p}<0$, the strong-interaction shift of the kaonic hydrogen atom 1s state should be repulsive. The three previous measurements, however, all reported an attractive shift. This discrepancy has been found to be impossible to reconcile in the conventional theoretical framework and has been called "the kaonic hydrogen puzzle." The quality of the previous x-ray measurements, however, was also called into question. The x-ray spectra suffered from a large background and low statistics, and hence x-ray signals were very difficult to identify. Therefore, a definitive experiment has been long awaited.

We have performed a new experiment at KEK to measure kaonic hydrogen x rays, using novel experimental techniques, and have succeeded in observing distinct K-series kaonic hydrogen x rays with good signal-to-noise ratio in the energy spectrum. A preliminary result has been reported [12]. In this paper, we present a full account of our experiment, including the details of the analysis that have not been previously reported.

II. EXPERIMENTAL METHOD AND APPARATUS

A kaonic hydrogen atom is formed when a negative kaon is stopped in hydrogen. A typical experimental procedure for the kaonic hydrogen x-ray measurement consists of exposing a hydrogen target to a low-energy kaon beam and detecting emitted x rays coincident with the incoming kaons by detectors placed in or around the target. In this experiment, in addition to these, tagging on two charged pions from the K^-p absorption was used in order to select appropriate events. The use of a gaseous target is another new feature of this experiment. A detailed description of the principles of the experiment and the experimental apparatus is given in a separate paper [13]. Here we give a short account relevant to the later description of the data analysis procedure.

The experiment was performed at the K3 low-energy separated beam line at the KEK Proton Synchrotron. A cross-sectional side view of the experimental apparatus is shown in Fig. 1. For later use, a Cartesian coordinate system (x,y,z) is defined with the z axis along the beam direction (the beam travels in the positive z direction), the x axis horizontal, and the y axis vertical. Also a cylindrical coordinate system (r,ϕ,z) is defined with the same definition of the z axis.

A. Beam counters

Negative kaons of 600 MeV/c from the K3 beam line were slowed down in a carbon degrader and were brought to rest in the hydrogen gas target. The timing of the incoming particle was measured with a scintillation counter B2. Three Lucite Čerenkov counters (LČ1, LČ2, LČ3) were used to reject contaminating pions in the beam. The LČ counters were of the total-internal-reflection type. Their efficiency was checked using time of flight between B2 and the scintillation counter B1 placed further upstream in the K3 channel, and was found to be $>99.99\%$ for pions. Placed after the carbon degrader were beam-defining counters B3 and B4, whose pulse height also served to identify kaons in the beam. The carbon degrader was surrounded by plastic scintillation counters (veto counters) to reject events in which a nuclear reaction with the kaon occurred in the degrader. The beam was tuned so that the kaon stopping yield was maximized. It was estimated from a Monte Carlo calculation that about 0.06% of the incoming kaons stopped in the hydrogen gas target. The average kaon intensity and the K/π ratio, both after the carbon degrader, were 8×10^3 per spill and 1/90, respectively. The spill duration was 2 s and the repetition rate was 1 spill per 4 s.

B. Target and Si(Li) detectors

A kaon stopped in hydrogen is trapped in an atomic orbit around a hydrogen nucleus, forming a kaonic hydrogen atom. The x rays from the kaonic hydrogen atoms were detected with lithium-drifted silicon [Si(Li)] x-ray detectors. The target density is a very important factor in designing the experiment: increasing the pressure increases the kaon stopping rate but also decreases the x-ray yield due to the Stark mixing effect. To obtain an optimum signal-to-noise ratio, a low-temperature pressurized gaseous target (100 K, 4 atm) was chosen as a compromise between the two. The density of the target was $\sim 0.94\times10^{-3}$ g/cm$^3\sim 10\rho_{\rm STP}$ ($\rho_{\rm STP}$ being the density at the standard temperature and pressure), giving an effective thickness of 50 mg/cm^2. In previous experiments, the Si(Li) detectors were separated from the liquid hydrogen target by beryllium windows, which not only attenuate x rays and distort the energy spectra, but also reduce the solid angle subtended by the Si(Li) detectors. In this experiment, the use of a gaseous target allowed us to place the Si(Li) detectors directly in the target volume, eliminating the need for windows. In order to obtain a large acceptance, we installed 60 Si(Li) detectors, each with an effective detection area of 200 mm^2. The average number of Si(Li) detectors used during the experiment, however, was kept at ~ 45 because if more than this number were in simultaneous operation, the reset of one Si(Li) detector induced serious cross talk in the other Si(Li) detectors. The reason for this behavior is still unknown. These windowless Si(Li) detectors were developed in cooperation with and provided by JEOL Engineering Co. [14]

At the downstream end of the target chamber, there was a hole with a beryllium window through which an ^{55}Fe source could illuminate the x-ray detectors for calibration purposes. The ^{55}Fe source was attached to one end of a rod so that it could be removed by pulling from outside the target. The ^{55}Fe source was inserted periodically when the beam was off to determine the calibration of each Si(Li) detector. The inner surface of the target chamber and the final Teflon degrader in the gas volume were lined with thin titanium foils. Titanium x rays (emitted when beam and other particles produced in various reactions passed through the foils) served as an in-beam energy calibration source.

C. Two-pion tagging system

The K^-p absorption, which occurs as the final stage of the atomic cascade of the kaonic hydrogen atom, produces various reaction products including high-energy γ rays. These high-energy γ rays, which are mainly due to the decays of π^0, Λ, and Σ^0, were a major background source in previous experiments. There are, however, reaction modes that have no γ rays in the final state: $K^-p\rightarrow\Sigma^\pm\pi^\mp$ followed by $\Sigma^\pm\rightarrow n\pi^\pm$. These modes (branching ratio $\sim 50\%$) are characterized by the presence of two charged pions with momenta higher than 150 MeV/c in the final state. There are no reaction modes in which γ rays are emitted along with two charged pions with momenta higher than 150 MeV/c. Thus, by tagging on two charged pions with momenta higher than 150 MeV/c, we can exclude all the reactions producing high-energy γ rays.

In addition, this two-pion tagging method serves to distinguish kaons stopped in hydrogen from those stopped in other materials and those which undergo in-flight decay or reactions in hydrogen. Since the lifetime of the charged Σ particle is short, the K^-p reaction and the Σ decay can be regarded as taking place approximately at the same point (several millimeters apart). Thus the K^-p reaction point can be obtained as the vertex of the trajectories of the two charged pions. Also, the time taken for the kaon to slow down and come to rest in hydrogen gas is several nanoseconds and can be measured as the time difference between the kaon injection into the target and the pion emission from the target. For stopped kaons, the time of flight (TOF) is determined uniquely as a function of the range in hydrogen. Thus, the requirement that the two-pion vertex occur in the hydrogen volume and have an appropriate time of flight clearly selects only kaons stopping in hydrogen and forming kaonic hydrogen atoms.

To achieve this two-pion tag, the target was surrounded with two layers of scintillation counter arrays T1 and T2 (for the timing of the outgoing particles) and two layers of multiwire proportional chambers (MWPC's) C1 and C2 (for reconstruction of the particle trajectories) as shown in Fig. 1. Both T1 and T2 were segmented into 16 in the ϕ direction in order to reduce the rate of multihits on the same counter and also to give a rough position in the ϕ direction. Each T2 counter was viewed by two photomultiplier tubes, one at each end, which gave a rough position in the z direction. C1 and C2 had essentially the same structure, except for their sizes. The anode wires were stretched parallel to the cylinder axis, whereas the cathode strips ran at angles of ±35° in C1 and ±45° in C2 with respect to the anode wires. With this configuration, it was possible to determine the z coordinate as well as the ϕ coordinate of the position of the avalanche by finding the intersection of the anode wire and the cathode strips which were fired. The anode and both cathode planes were read out by the charge-division method. The outermost layer was an array of water Čerenkov counters (WČ), which served to reject false triggers caused by $e^{\pm}$, which are mainly produced by γ-ray conversion. The water Čerenkov array was also segmented into 16 in the ϕ direction. Because the thickness of the T2 counters was 1 cm, the pulse height information was also used to distinguish between pions from the $K^{-}p$ reaction ($\beta \sim 0.8$) and $e^{\pm}$ produced by γ-ray conversion ($\beta \sim 1.0$). This two-pion tagging system (T1, T2, C1, C2, and WČ) subtended a solid angle of about 70% at the target chamber, thus providing an acceptance of 50% to events with two charged pions.

D. Trigger and data acquisition

For the trigger we required that the incoming particle be a kaon and that there be at least two particles outgoing from the target. Thus the trigger condition was $K\times(T1\geqslant 2)\times(T2\geqslant 2)$, where $K=B2\times\overline{(\text{LČ1}\cup\text{LČ2}\cup\text{LČ3})}\times B3\times B4\times\overline{\text{VETO}}$. Note that neither the Si(Li) x-ray detectors nor the water Čerenkov counters were included in the trigger. The typical trigger rate was 250 per spill and about 70% of the triggers were accepted by the data aquisition system. For each trigger, the following information was recorded: the pulse height information and the timing information for the beam counters (B2, B3, B4) and the Lucite Čerenkov counters (LČ1, LČ2, LČ3), the timing information for each T1, the pulse height and timing information for each T2 and WČ, the pulse height information for the MWPC's, and the pulse height and the timing information for each Si(Li) detector. The signals from the Si(Li) detectors were processed by Ortec 570 shaping amplifiers set to 10-μs Gaussian shaping and incorporating dc base line restoration circuitry. The pulse height information (the output of the shaping amplifier) of each Si(Li) detector was recorded by a peak-sensing analog-to-digital converter (ADC) with a 20-μs gate width. The timing information, which was used to reject pileups as well as to select x-ray signals in coincidence with the incoming kaons, was recorded by a multihit (up to 16 hits) long-range (64-μs time gate) LeCroy 2277 time-to-digital converter (TDC). The timing of beam pions striking the beam counters was also recorded with a long-range TDC in order to reject later, in the off-line analysis, the Si(Li) signals induced by beam pions. Data were collected for three periods of time, each about 2 weeks long, for a total of 6 weeks over the period from February 1995 to June 1995. In total, 1.18×10^{8} events were accumulated over 763.2 h.

III. DATA ANALYSIS

A. Overview

The detector analysis procedure can be divided into two major parts: selection of ‘‘valid events’’ and creation of x-ray energy spectra by collecting Si(Li) signals for such valid events. Here ‘‘valid events’’ are those in which the incoming kaon stops in the hydrogen target and two charged pions are detected by the two-pion tagging system.

Valid events were identified by going through the following procedure for each event: (1) Identify the kaon in the beam using information from the beam counters. (2) Analyze the MWPC data to identify two outgoing particle trajectories and reconstruct the vertex point. (3) Identify whether the two outgoing particles were pions, using the WČ ADC and the T2 ADC information. (4) Identify whether the kaon was stopped in the hydrogen target (=hydrogen stop) by looking at the correlation between the vertex point and the time of flight between B2 and T2 (TOF cut).

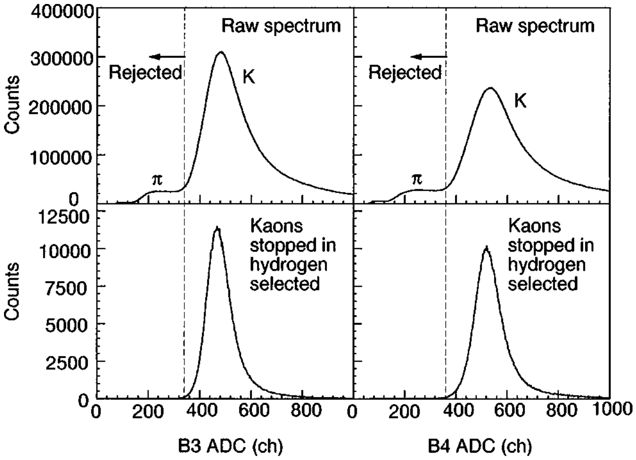

FIG. 2. ADC spectra of the beam defining counters. For each of B3 (left) and B4 (right), the raw spectra (top) and the spectra with stopped kaons in hydrogen selected (bottom) are shown. We rejected events for which either the B3 ADC is below 340 channel or the B4 ADC is below 360 channel.

For such selected events, the Si(Li) data were analyzed through the following steps: (1) Select those Si(Li) detectors which had a hit coincident with the incident kaon timing. (2) Reject data from Si(Li) detectors which were hit by outgoing pions. (3) Reject Si(Li) data time correlated with beam pions. Finally, collecting the selected Si(Li) data, an x-ray energy spectrum was obtained.

Before undertaking this event-by-event analysis, the Si(Li) detector calibration parameters were determined using the manganese x-ray peaks from the data taken with the ^{55}Fe source inserted and the beam off and the titanium x-ray peaks from the data taken with the beam on.

B. Event selection

1. *Identification of kaons in the beam*

Although the LČ counters had a high efficiency for vetoing pions in the beam at the trigger level, there was still some pion contamination in the trigger caused by the imperfections in the electronics. This remaining contamination was rejected off line by using the pulse height information from the LČ counters. Also, since slow (stopping) kaons and fast pions had quite different energy deposits on B3 and B4, the pulse height information of B3 and B4 was used to further reduce the pion contamination. In Fig. 2, the pulse height spectra of B3 and B4 are shown. At the top are the raw spectra without any cuts. At the bottom, the same spectra are shown but with stopped kaons in hydrogen selected using the TOF cut (B2-T2 time-of-flight information using the method described in Sec. III B 4). It can be seen that the identification of the kaon in the beam by the beam counters is not crucial since the stopped kaon selection eliminates virtually all the pions in the beam.

2. Vertex reconstruction I: Single combination events

Since the trigger required that the T1 and T2 arrays each have two or more hits, each of C1 and C2 probably had two or more hits in an event. The hits on the MWPC's may be due to particles created by a K^--nuclear reaction in or around the target, or may be due to beam pions accidentally coincident with the incoming kaon. The hits on the MWPC's which were due to the two charged pions from kaons stopped in hydrogen must be selected and their trajectories determined.

Since the MWPC's were read out by the charge division method, a hit on a MWPC shows up as two adjacent preamplifiers fired on each of the anode and the two cathode planes. The first step in the vertex reconsctruction was therefore to seek pairs of fired preamplifiers on each plane. The ratio of the charges collected by the two preamplifiers of such a pair determines a line on which the hit on the MWPC is located. If there was only one hit in each event, the position of the hit would be obtained by finding the intersection of three such lines (one from each plane). However, in our case, there were in general more than two particles hitting the MWPC's. If two particles hit the MWPC's in two adjacent sectors of charge division, then information from one or more planes may be unresolvable, and thus useless in reconstructing the vertex. Thus the intersection of only two lines was also taken as a candidate for the position of the hits. For C2, the z position of the intersection of two lines was required to be consistent with that obtained by the T2 counters.

The position of one candidate hit from C1 and one from C2 gives a candidate particle trajectory. A natural way to find the correct position of hits and their correct combinations would be to look for the combination of candidate hits which gives the two trajectories for which the miminum distance between the tracks is the smallest among all the possible combinations. In our case, however, such a combination may not always be the correct one for the following two reasons: (1) The two charged pions are not created at the same point: the points where they are created are separated by several milimeters because the charged Σ travels several milimeters before decaying. (2) The vertex resolution of our tracking system for two-charged-pion tracks was estimated to be as large as 10 mm, by a Monte Carlo study, due to the multiple scattering effects in the target chamber and the vacuum vessel.

Thus we also used the B2-T2 time-of-flight information (use of this information to select stops in hydrogen will be described in Sec. III B 4) to select a valid combination. We will come to this point later in Sec. III B 5 and here we only deal with events with only one possible combination of candidate hits.

In Figs. 3 and 4, we show the x-y and z distributions of the positions of the vertices for such events. In Fig. 3, we see the Si(Li)-detector holder and the Si(Li) detectors at the top and the bottom of the holder. In Fig. 4, we see the peaks corresponding to the front and the back walls of the target system. From the fit to the Teflon plate peak, the vertex spatial resolution was determined to be 9 mm rms. Also, in Fig. 5, we show the vertex distribution in the r direction. In Fig. 5 (top), we clearly see events corresponding to kaons stopping in the Si(Li) detectors and their holder. With the TOF cut, the kaons stopping in the Si(Li) detectors and their holder are suppressed considerably. The fiducial volume chosen for analysis, -40 mm $<z<300$ mm and $r<125$ mm, was chosen to maximize the statistical precision of our result.

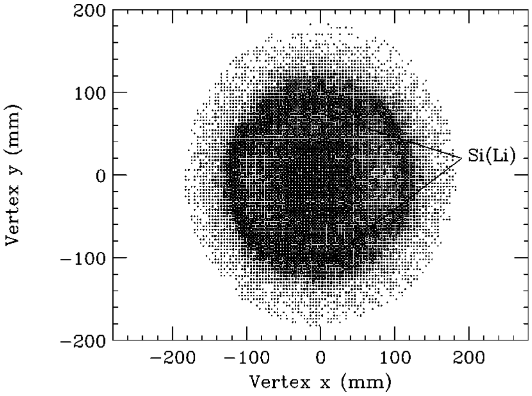

FIG. 3. Distribution of the vertex in the x-y plane. For this plot, vertices with $0\ \mathrm{mm}<z<300$ mm are selected and the two-pion cut (described in Sec. III B 3) is applied.

3. Selection of two-pion events

The trajectories reconstructed as described above contain electrons and positrons as well as pions. The π/e separation can be achieved by using the pulse height information of the T2 counters and the WC counters. Figure 6 (left) shows the correlation between the pulse heights of the WC counter and the T2 counter along the same particle trajectory. In the figure, regions corresponding to individual pion and electron (or positron) tracks are seen along with events in which both an electron and a positron created by γ conversion pass through corresponding detectors $(2e^{\pm})$. We required that both of the trajectories fall in the region enclosed by the solid curve.

4. Stopped K^- identification: Kaon ''range-TOF'' analysis

Since the target density is quite low, far more kaons undergo ''in-flight'' decay in the hydrogen target than are stopped. Although most of the in-flight K^- decays are rejected by the two-pion cut which has just been described, it is important to further reduce the K^- decay contamination in

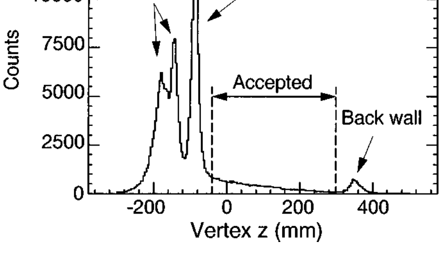

FIG. 4. Distribution of the vertex in the z direction. For this plot, vertices with $r<80$ mm are selected and the two-pion cut (described in Sec. III B 3) is applied.

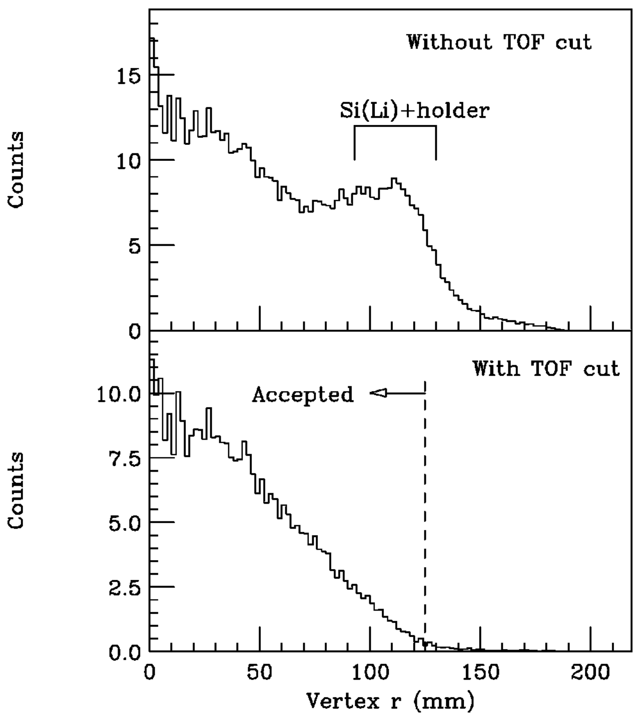

FIG. 5. Distribution of the vertex in the r direction (weighted by $1/r$) without the TOF cut (top) and with the TOF cut (bottom). For this plot, vertices with $0<z<300$ mm are selected and the two-pion cut (described in Sec. III B 3) is applied. We required $r<125$ mm.

order to achieve a good signal-to-noise ratio. Also, in-flight K^-p reactions cannot be distinguished from stopped kaons by the two-pion cut.

Shown in Fig. 7 is a contour plot of the time difference between B2 and T2 (T2 TDC−B2 TDC) against the z value of the vertex. For this plot, events with vertices with $r<80$ mm were selected and the two-pion cut has already been applied. Since the particles detected by the T2 counter are much faster than slowing-down kaons, the time difference between B2 and T2 is to a good approximation the time of flight of the slowing-down kaons. In the figure, peaks corresponding to the front and the back walls of the target system are seen and, in the hydrogen region, stops are clearly separated from decays or reactions in flight. Events in the region enclosed by the solid lines were selected as stopped kaons.

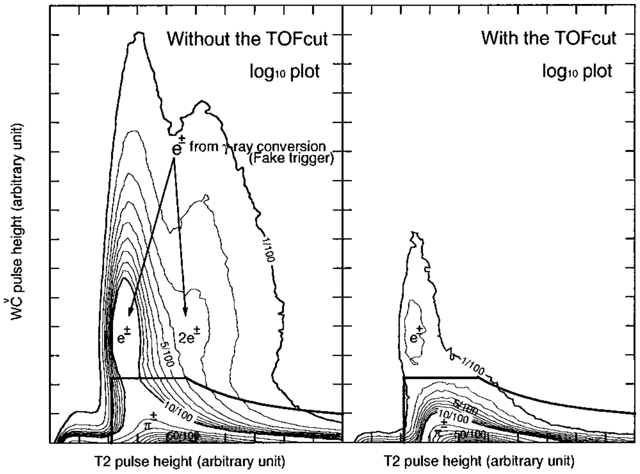

FIG. 6. The W̌C pulse height versus the T2 pulse height, without any cuts (left) and with the TOF cut (right). It can be seen that the e^+/e^- events are suppressed with the TOF cut.

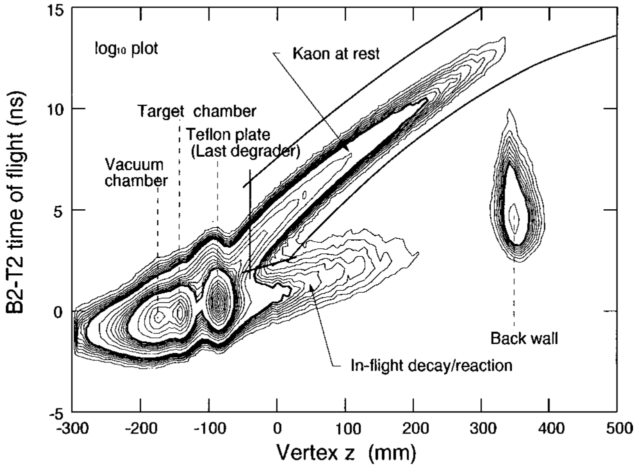

FIG. 7. Time difference between B2 and T2 versus vertex z. It can be seen that hydrogen stops are well separated from decays and reactions in flight. For this plot, events with vertices with $r<80$ mm are selected and the two-pion cut is applied. We accepted the events in the region enclosed by the solid curves.

This clear separation can be understood by looking at Fig. 8. The curves drawn in the figure are trajectories of the incoming kaons having different initial velocities when entering the hydrogen target. The curves are drawn in steps of $0.01c$, with the highest being $\beta=0.4$. The slope of the curve is the reciprocal of the velocity. As the kaon proceeds, it loses its kinetic energy and the curve bends upwards. After a time interval which is uniquely determined by the incident velocity (neglecting the range straggling and multiple scattering inside the target), the kaon comes to rest, if it has not decayed, and the slope of the curve becomes infinite as the trajectory terminates. The larger the initial velocity, the longer the time it takes the kaon to come to rest and the farther away from the entrance wall the stopping point is. This is why the stopped kaons distribute as in Fig. 7. The clear ridge that has been identified as kaons at rest is an

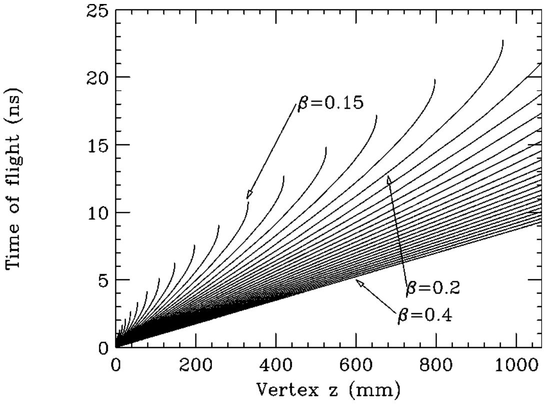

FIG. 8. Calculated trajectory for kaons in hydrogen with different initial velocity. Compare to the "time-of-flight vs vertex z" plot shown in Fig. 7.

indication of the effectiveness of the 2π trigger. In Fig. 6 (right), the WC ADC versus T2 ADC plot with this TOF cut is shown. It can be seen that the $e^{\pm}$ events are significantly suppressed.

5. Vertex reconstruction II: Multiple combination events

In order to select the correct position of hits on the MWPC's from the candidate hits and find their correct combinations even for events with multiple combinations, the information from the range-TOF analysis was also used. The following procedure was adopted to identify the correct combination of the candidate hits: the minimum intertrack distance between the two particle trajectories (DIFF) was required to be less than 60 mm. If there is more than one such combination, the one with an appropriate range-TOF correlation for a stopped kaon was chosen. When this procedure selected more than one combination, the one with the smallest intertrack distance was chosen.

The largest allowed value for the DIFF was determined to be 60 mm by making a sample of events with only one possible combination of candidate hits and an appropriate range-TOF correlation for a stopped kaon, and looking at the DIFF distribution for such events. By using this procedure for finding the correct combination of candidate hits, we achieved almost twice the analysis efficiency [analysis efficiency = (the number of valid events recognized as valid)/(the number of valid events)] for hydrogen-stop events than obtained by simply seeking the combination giving the two trajectories with the smallest minimum intertrack distance.

6. Summary of event selection

By the method described above, 7.9×10^5 valid events were selected out of the 1.18×10^8 events which had satisfied the trigger condition and had been recorded on the magnetic tape.

Using this number of valid events, the efficiency of the two-pion tracking system (including the analysis efficiency) for the two-pion events was estimated to be ~40%. On the other hand, the measured efficiency of the tracking system for cosmic rays was slightly greater than 50%. Here the efficiency for cosmic rays was defined to be the ratio of the number of events in which both C1 and C2 have two hits, all four of which can be fitted by a straight line, to the number of events in which the uppermost and lowermost T2 counters fire.

Considering that under the beam-on condition the MWPC efficiency decreases due to the multiparticle hits in the same or adjacent sectors (mostly due to beam pions), an efficiency of ~40% for the two-pion events is reasonable.

C. X-ray detector analysis

1. Energy calibration I: Calibration of the individual detectors

First, for each data set (set of data taken under one running condition, which typically lasted for several days to 2 weeks), the energy calibration parameters for individual x-ray detectors were determined using the data which were taken before and after the runs with the ^{55}Fe source inserted and with the beam off. In this process, the pedestal was assumed to be the zero energy point. In Fig. 9, ADC spectra of some typical detectors for ^{55}Fe data are shown. Titanium as well as manganese x rays from ^{55}Fe can be seen because x rays from ^{55}Fe excite titanium K-shell electrons.

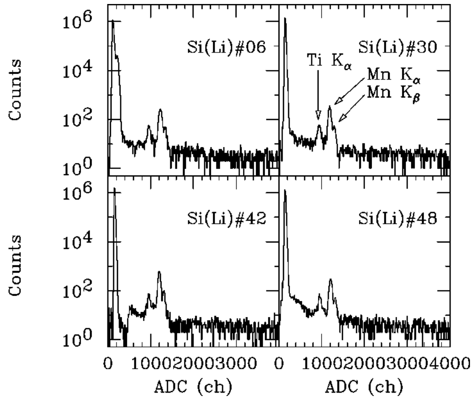

FIG. 9. Typical x-ray ADC spectra of single Si(Li) detectors for data with the ^{55}Fe source inserted and the beam off. Manganese $K\alpha$ and $K\beta$ x rays from the ^{55}Fe source (energy=5.895 keV and 6.490 keV, respectively) and titanium $K\alpha$ x rays (energy=4.511 keV for $K\alpha_1$) can be seen.

In order to demonstrate the linearity of our x-ray detection system, the deviation of the position of each x-ray line from the position obtained using the calibration parameter determined by the position of the manganese $K\alpha$ line and the pedestal position is shown in Fig. 10. The linearity is better than several ×0.1% for the beam-off condition, using the pedestal as the zero energy point.

In Fig. 11, an x-ray spectrum summed over all Si(Li) detectors whose resolution was better than 400 eV for ^{55}Fe data is shown. The individual detectors had been energy calibrated. On average, the number of such good Si(Li) detectors was ~25 out of the ~45 that were used.

2. Timing selection

Since we used a secondary kaon beam which was contaminated by pions, good timing resolution of the x-ray signal is indispensable in reducing the accidental background due to pions. Also, in order to avoid distortion of x-ray energy spectra, any x-ray signal which is piled up with other signals must be rejected.

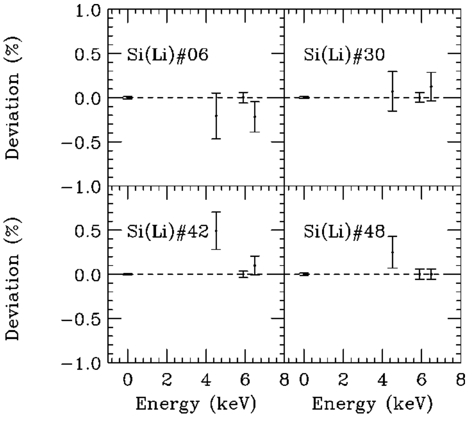

FIG. 10. Deviation of the position of each x-ray line from the position obtained using the calibration parameter determined by the position of manganese $K\alpha$ line and the pedestal position.

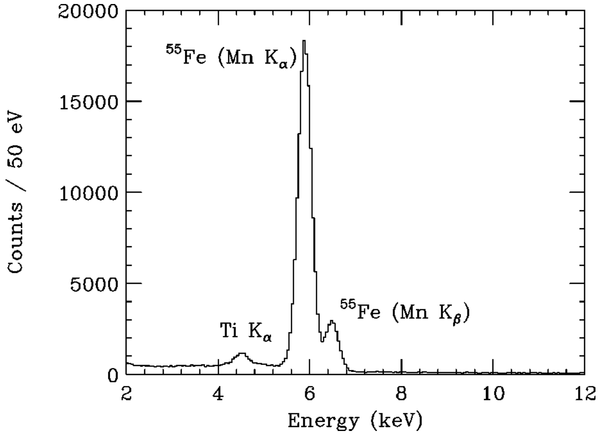

FIG. 11. Typical summed x-ray energy spectrum of data with the ^{55}Fe source inserted and the beam off. An energy resolution of 361 ± 1 eV (FWHM) at 5.895 keV was obtained by a fit to the Mn $K\alpha$ peak.

In Fig. 12, a typical distribution of the multihit TDC multiplicity of a Si(Li) is shown. Here the TDC multiplicity is defined to be the number of TDC hits on a single Si(Li) detector in one event (the time gate width is 64 μs). It is seen that for most of the events, the multiplicity is 0 or 1: for any Si(Li) detector, the ratio of events with multiplicity $\geqslant 2$ to all the events is less than 1%. In order to avoid pileups, we rejected data with multiplicity $\geqslant 2$.

In order to achieve a good signal-to-noise ratio, all the individual Si(Li) detectors were time-walk corrected for each data set. A function of the following form was used:

$$\mathrm{TDC}_j = p_{1j} + p_{2j} \times \mathrm{ADC}_j^{\,p_{3j}},$$

where p_{1j}, p_{2j}, and p_{3j} are parameters for each detector determined from a fit to the data.

The time-walk-corrected time spectrum summed over all the good Si(Li) detectors for the energy range 2–20 keV with the TOF cut applied is shown in Fig. 13 for a typical data set. The time resolution after the time-walk correction was 290 ± 10 ns [full width at half maximum (FWHM)]. We defined a ''prompt time gate'' and x-ray signals within this gate were taken as being coincident with the kaon. The gate width for a typical data set was ±360 ns. In the figure, we see a bump at around 3000–4000 ns which is discussed in the next section.

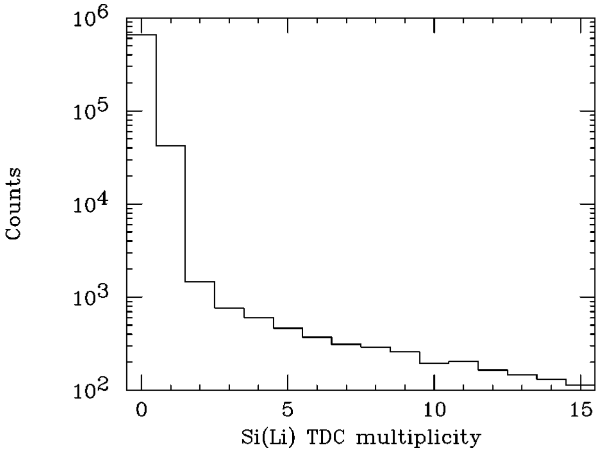

FIG. 12. Typical TDC multiplicity distribution for a Si(Li). For most of the events, the multiplicity is 0 or 1.

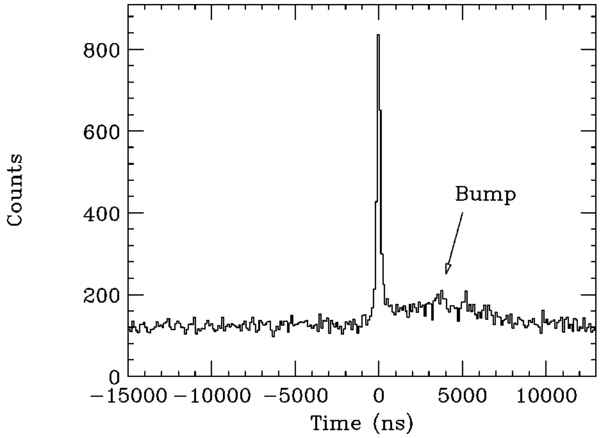

FIG. 13. The time-walk-corrected time spectrum summed over all the good Si(Li) detectors for the energy range 2–20 keV with the TOF cut applied for a typical data set. A bump is seen at around 3000–4000 ns.

3. Rejection of data of Si(Li) detectors hit by outgoing pions

Data were rejected for Si(Li) detectors through which the outgoing particle trajectories obtained by the MWPC analysis went.

In most cases, a Si(Li) detector which was hit by an outgoing charged particle gave a huge pulse which did not affect the Si(Li) x-ray spectrum in the energy region of interest. However, we found that the bump found in Fig. 13 disappears when such Si(Li) data are rejected. One explanation is that the bump is due to pions hitting the Si(Li) detector in the inefficient region where it takes time to collect charges deposited. In fact, the timing of the signals resulting in the bump has such an energy dependence that, the lower the energy, the later the signal even after applying the time-walk correction developed for ''normal'' signals. In Fig. 14, the time-walk-corrected Si(Li) time spectrum is plotted as a solid-line histogram, rejecting data of Si(Li) detectors which are hit by outgoing particles. The prompt time gate is shown as dashed lines. Now the time spectrum is quite flat except for the peak at $t=0$. The flat part is mainly created by the continuous beam pions. Thus from an x-ray spectrum gated on the delayed and advanced part of the time spectrum, the background due to accidental beam-pion hits can be estimated.

4. Rejection of data time correlated with beam pions

To reduce accidental background due to beam pions, the timing of these pions was monitored using a multihit (up to 16 hits) long-range (16 μs) TDC. Si(Li) data that were time correlated with pions were rejected. The TDC was operated in the common stop mode and the stop signal to the TDC was the trigger signal delayed by 8 μs. Thus the ''beam-pion timing monitor'' covered the time range of ±8 μs with respect to the trigger timing. Shown as a dashed-line histogram in Fig. 14 is the Si(Li) time spectrum after the beam-pion cut is applied. It is plotted only for the time range

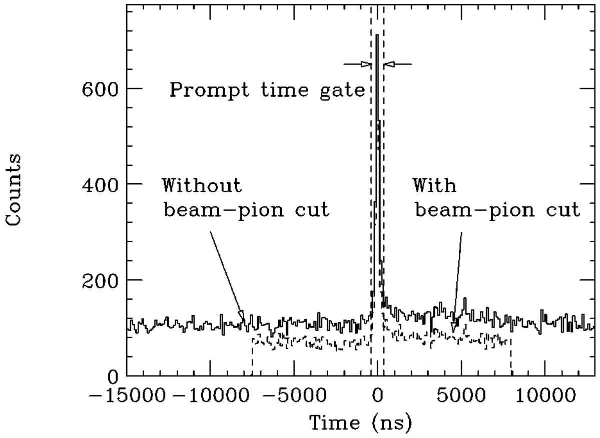

FIG. 14. The time-walk-corrected time spectrum summed over all the good Si(Li) detectors for the energy range 2–20 keV with the TOF cut applied for a typical data set. The data of the Si(Li) detectors which are hit by outgoing particles are rejected. It is seen that the bump disappeared. Shown as a dashed histogram is the time spectrum with the beam-pion cut. Dashed lines indicate the prompt time gate.

of the TDC. This time range was not made longer in order to keep the multiplicity to a reasonable value compared to the maximum number of allowed hits of the TDC.

5. Energy calibration II: In-beam stability

The titanium x rays were used to monitor the gain and its stability when the beam was on. Irrespective of the data set, when the x-ray data are analyzed using the calibration obtained in Sec. III C 1 from the beam-off ^{55}Fe source data, the titanium x-ray peak in the summed spectrum appear at positions about 2% higher than those for the beam-off data while the width of the peak remains more or less the same. We interpreted this as a change in the gain, not a change in the zero-energy point, and accordingly rescaled the factor to convert ADC channel to energy. The validity of this procedure was checked by processing in the same way the data taken with the beam on and copper as well as titanium foils attached on the inner surface of the target chamber. The energy of the copper $K\alpha_1$ x ray, which is the most predominant, is 8.048 keV. After rescaling the ADC-energy conversion factor to bring the titanium peak to the correct energy, the energy of the copper x-ray peak was within 0.4% of the known value. This discrepancy is much smaller than other relevant errors in this experiment.

In Fig. 15, we show the x-ray spectrum with the time cut applied, summed over all the good Si(Li) detectors and all the data sets. It should be noted here that this summed spectrum is smooth even in the region below 3 keV although TDC threshold levels of the individual detectors distribute in this region and the detection efficiency in this region is not known. By fitting to the titanium peak ($K\alpha_1$, $K\alpha_2$, and $K\beta$) in this spectrum with the known intensity ratios [15], an energy resolution of 407 ± 7 eV (FWHM) was obtained at 4.511 keV for the beam-on condition. This value for the energy resolution of our x-ray detector was used when interpreting experimental x-ray spectra in Sec. IV.

Since the energy resolution is predominantly determined by the microphonic noise (noise due to the feedback capacitance of the preamplifier picking up the vibration caused by boiling liquid nitrogen), it is expected that the energy dependence is negligible in the region of interest. The energy dependence was estimated by assuming that the energy resolution is given by

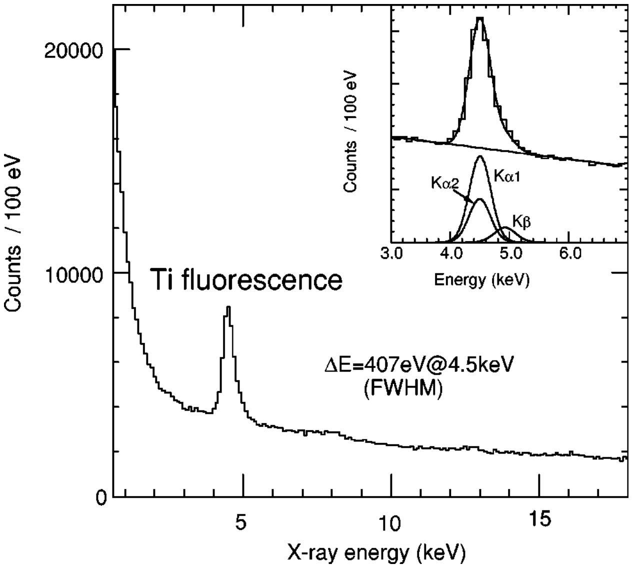

FIG. 15. X-ray spectrum obtained with the prompt time cut. No structure is seen except for the titanium x-ray peak and a small bump at around 8 keV. An energy resolution of 407 ± 7 eV (FWHM) at 4.511 keV for the beam-on condition was obtained by fitting to the titanium peak (see inset).

$$\Delta E\ \ (\mathrm{FWHM}) = 2.35\omega\sqrt{W_N^2 + \frac{FE}{\omega}}, \tag{2}$$

where W_N represents the contribution of noise to the resolution (independent of the x-ray energy), E is the x-ray energy, F is the Fano factor (≈ 0.12 for Si), and ω is the amount of energy necessary to create an electron-hole pair (3.68 eV for Si). Obtaining W_N by using the resolution at 4.511 keV, the energy dependence of the energy resolution can be calculated using Eq. (2). The difference in the energy resolution at 4.511 keV and at 10 keV is only about 4%. To a very good approximation, a constant energy resolution can be used over the range of interest when x-ray spectra are fitted in Sec. IV.

6. Cross-talk problem

Even with the number of Si(Li) detectors in operation maintained at ~45, occasionally, a reset of one Si(Li) detector induced a signal in other Si(Li) detectors. If this strange-shaped pulse adds to a real x-ray signal, the resultant energy spectrum is distorted. The effect of cross-talk should therefore be eliminated to obtain an undistorted energy spectrum. These cross-talk events are characterized by high multiplicity. By looking at the ADC multiplicity [estimated as the number of Si(Li) detectors with an ADC above a certain threshold (~1 keV)], cross-talk events can be rejected.

Figure 16 is a plot of Si(Li) energy versus Si(Li) multiplicity. For this figure, all the cuts described above except for the beam-pion cut are applied, i.e., the stopped kaon selection by the TOF cut and the two-pion cut, the Si(Li) timing

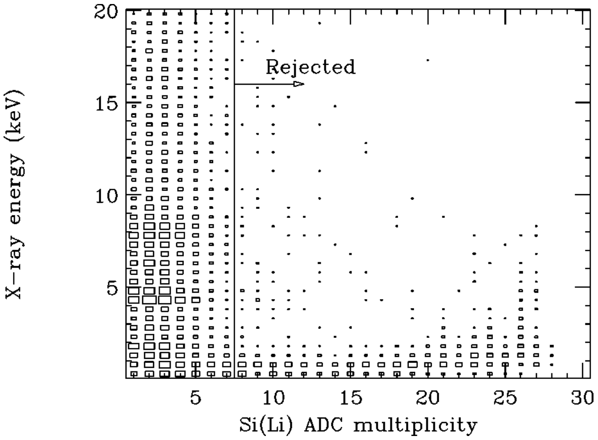

FIG. 16. Si(Li) energy versus Si(Li) multiplicity. Those events with multiplicity $\geqslant 8$ were rejected as cross-talk events.

selection, and the outgoing and beam-pion cuts. Events with multiplicity $\geqslant 8$ were rejected as cross-talk events.

IV. ANALYSIS AND INTERPRETATION OF THE X-RAY SPECTRUM

A. Determination of the 1*s* shift and width

1. Description of the spectral region

The solid-line histogram in Fig. 17 shows the ''prompt-time-gate spectrum'' obtained after applying all the event-selection cuts. Also shown as a dashed-line histogram is the ''off-time-gate'' spectrum obtained by gating on the delayed and advanced part of the x-ray time spectrum in Fig. 14, normalized by the ratio of the gate widths.

The 4.5-keV titanium x rays used for calibration are clearly seen in both prompt and off-time-gate spectra. There were ~0.25 beam pions passing through B3 during the 720-ns prompt-time-gate width, whereas there is always one kaon in the prompt time gate. The difference in the titanium x-ray intensities between the prompt-time-gate and the off-time-gate spectra is somewhat larger than the ratio of the rates of kaons and pions (=1/0.25). This is due to different *K*-shell ionization and excitation cross sections for the fast pion and the slow stopping kaon.

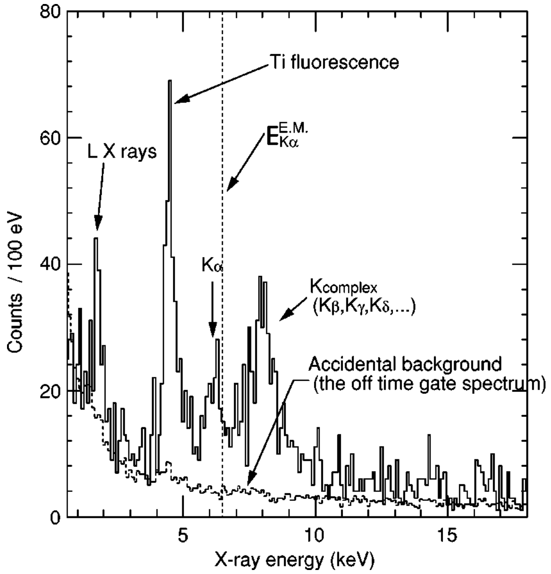

FIG. 17. X-ray spectrum obtained after applying all the cuts. Also shown in dashed-line histogram is the off-time-gate spectrum (see text). The dashed line indicates the pure electromagnetic energy of the $K\alpha$ x ray.

The off-time-gate spectrum has no structure except for the small titanium peak, as expected. However, the accidental background seen in the off-time-gate spectrum does not fully account for the background observed in the prompt-time-gate spectrum. This difference may be caused by the two outgoing charged pions passing through the target. Bremsstrahlung from the δ rays produced by the pions is a possible mechanism.

The structure in the 6–9 keV region is attributed to the kaonic hydrogen *K* x-ray series. The peak around 6 keV is $K\alpha$ x rays and the structure around 8 keV is K_{complex} that consists of the $K\beta$ and higher x rays. Comparison of Figs. 15 and 17 reveals the dramatic improvement in the signal-to-noise ratio resulting from the event selection requirement. The dashed line in Fig. 17 indicates the pure electromagnetic energy of the $K\alpha$ x ray. Clearly, the kaonic hydrogen $K\alpha$ peak is located on the lower-energy side of its pure electromagnetic value, and the shift is thus *repulsive*. The pure electromagnetic energies of kaonic hydrogen *K*-series x rays are listed in Table I.

2. Fitting function and background estimation

In order to obtain the position and the width of the $K\alpha$ peak, the spectrum was fitted with an appropriate function. The maximum likelihood method was used in fitting. Assuming that the number of counts in each bin is Poisson distributed, we determined the parameters of the fitting function by minimizing the Poisson likelihood chi square [18]

$$\chi_{\mathrm{P}}^2=\sum_i \left[2(N_i^{\mathrm{f}}-N_i^{\mathrm{obs}})+2N_i^{\mathrm{obs}}\ln(N_i^{\mathrm{obs}}/N_i^{\mathrm{f}})\right], \tag{3}$$

where N_i^{obs} is the observed number of events in the ith bin and N_i^{f} is the number predicted from the fitting function. The change in a parameter value which causes a change in χ_{P}^2 by unity was assigned as the statistical error of the parameter.

Since the energy of x rays which have a natural line width was measured using detectors whose response can be approximated by a Gaussian function, each *K*-series line is represented by a Lorentz function with a width corresponding to the natural width convoluted by a Gaussian function with a width corresponding to the detector resolution (the Voigt function). The Voigt functions used were calculated from the complex error function [19], of which the numerical evaluation was performed using the algorithm by Gautschi [20].

The shift and width being appreciable only in the 1*s* state, the energy spacing between the different *K*-series lines is determined by the electromagnetic value and all the *K*-series lines have the same increase in width. Thus, we used the following function for the kaonic hydrogen x-ray part of the fitting function:

$$I_K(E)=\sum_{n=2}^{\infty} A_{np\to 1s}V(E,E_{np\to 1s}^{\mathrm{E.M.}}+\Delta E_{1s},\Gamma_{1s},\sigma), \tag{4}$$

TABLE I. Calculated values of the kaonic hydrogen electromagnetic energies (top) and K x-ray energies (bottom left) [16]. Vacuum polarization, the finite size effect, and the relativistic effect were included. The uncertainty of the energy of each atomic level due to the numerical error is about an electron volt for the $1s$ state and a few tenths of an electron volt for the other states. This difference is due to the unknown charge distribution of the kaon (the uncertainty due to this is indicated in parentheses). Also, the uncertainty of the kaon mass taken from Ref. [17] (493.677 ± 0.016 MeV) causes a $1s$ energy uncertainty of 0.0003 keV. Consequently, the transition energies have an uncertainty of about one electron volt. Calculated L x-ray energies are also shown (bottom right). When calculating the L x-ray energies, corrections to all the d-state energies were neglected.

State	Total energy (keV)	Nonrelativistic energy (keV)	Vacuum polarization (keV)	Relativistic correction (keV)	Finite size effect (keV)	Higher-order vacuum polarization (keV)
$1s$	8.6339	8.6128 (± 0.0003)	$+0.0219$	$+0.0006$	-0.0016 (± 0.0006)	$+0.0002$
$2p$	2.1540	2.1532	$+0.0008$			
$3p$	0.9572	0.9570	$+0.0002$			
$4p$	0.5384	0.5383	$+0.0001$			
$5p$	0.3445	0.3445				
$6p$	0.2392	0.2392				
$7p$	0.1758	0.1758				
$8p$	0.1346	0.1346				

Transition	X-ray name	Energy (keV)	Transition	X-ray name	Energy (keV)
$2p \rightarrow 1s$	$K\alpha$	6.4799	$3d \rightarrow 2p$	$L\alpha$	1.1972
$3p \rightarrow 1s$	$K\beta$	7.6767	$4d \rightarrow 2p$	$L\beta$	1.6159
$4p \rightarrow 1s$	$K\gamma$	8.0955	$5d \rightarrow 2p$	$L\gamma$	1.8097
$5p \rightarrow 1s$	$K\delta$	8.2894	$6d \rightarrow 2p$	$L\delta$	1.9150
$6p \rightarrow 1s$	$K\epsilon$	8.3947	$7d \rightarrow 2p$	$L\epsilon$	1.9784
$7p \rightarrow 1s$	$K\zeta$	8.4581	$8d \rightarrow 2p$	$L\zeta$	2.0196
$8p \rightarrow 1s$	$K\eta$	8.4993	$9d \rightarrow 2p$	$L\eta$	2.0479
$\infty \rightarrow 1s$	$K\infty$	8.6339	$\infty \rightarrow 2p$	$L\infty$	2.1542

where $V(E, E_0, \Gamma, \sigma)$ represents a properly normalized Voigt function with E_0, Γ, and σ being its central position, Lorentzian, and Gaussian widths, respectively, and A its amplitude. The electromagnetic transition energies $E^{\mathrm{E.M.}}_{np \rightarrow 1s}$ are listed in Table I.

The intensity of each line (and of course the intensity ratios among the lines) depends on the details of the cascade process, including the initial capture process and collisions with surrounding hydrogen atoms, and cannot be calculated in a model-independent way. Nevertheless, it is generally true that for large n, the contribution from the np to $1s$ transition can be safely ignored, because $E1$ transitions with a large Δn are quite improbable. The values of $A_{np \rightarrow 1s}$ were set to 0 for $n \geqslant 9$ in agreement with results obtained using the cascade code of Borie and Leon [21]. For σ, the detector resolution of 407 eV (FWHM), which was obtained in Sec. III C 5, was used. The energy dependence was ignored. The systematic error in the final fitted results due to the uncertainty in the detector energy calibration and that associated with ignoring the energy dependence of the x-ray detector resolution will be discussed in Sec. IV A 5.

Assuming that the background is a smooth function of energy, we determined the shape of the background by fitting a quadratic function to the prompt-time-gate spectrum in the energy region from 3 to 4 keV and from 10 to 18 keV, where no structure is expected.

For the titanium x-ray peak, three Gaussian functions with a width of the detector resolution [407 eV (FWHM)] and with the known intensity ratios [15] for the $K\alpha_1$, $K\alpha_2$, and $K\beta$ were used.

3. Iterative fit

In order to avoid uncertainties due to the unknown intensity ratios of the individual K-lines and thus minimize the source of systematic uncertainty, we used only the $K\alpha$ peak, which is well separated from other lines, at the cost of an increased statistical uncertainty to derive the shift and width. However, the contribution of the K_{complex} must be estimated. Thus, the following iterative procedure was adopted to fit the spectrum (see Fig. 18).

(1) A region $R_{K\alpha}$ around the $K\alpha$ peak was fitted with a single Voigt function for the $K\alpha$ peak and a background to determine the shift and width. The free parameters were the shift, the width, and the amplitude of the $K\alpha$ peak.

(2) The 3–10 keV region was fitted with the full function keeping the shift and width fixed and allowing the amplitude of each line to vary.

(3) The region $R_{K\alpha}$ was refitted, this time using the full function and treating the tail of K_{complex} and the titanium peak as part of the background. The shift, width, and amplitude of the $K\alpha$ peak were free parameters. All the param-

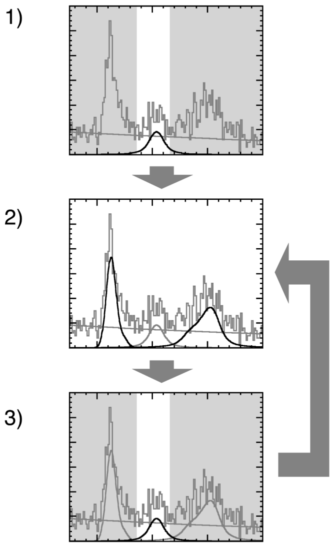

FIG. 18. Iterative fit procedure. (1) Fit a region $R_{K\alpha}$ around the $K\alpha$ peak with a single Voigt function for the $K\alpha$ peak and the background to determine the shift and width. The free parameters are the shift, the width, and the amplitude of the $K\alpha$ peak. (2) Fit the 3–10 keV region with the full function with the shift and width fixed and the amplitude of each line allowed to vary. (3) Again fit the region $R_{K\alpha}$, this time using the full function treating the tail of the K_{complex} and the titanium peak as part of the background. The shift, width, and amplitude of the $K\alpha$ are free parameters. All the parameters for the K_{complex} and the titanium peak are fixed. (4) Repeat steps (2) and (3) until the values of the shift and width converge.

eters for K_{complex} and the titanium peak were fixed (note that separate values of the shift and width were used for $K\alpha$ and K_{complex} at this step, although not physical).

(4) The last two steps were repeated until the values of the shift and width converged.

The convergence was quite fast (see Table II) and five iterations were sufficient. Also, the contribution from the tail of the K_{complex} to the $K\alpha$ fit was small.

There is a certain arbitrariness in the choice of the region $R_{K\alpha}$, which may cause a bias in the fitted result. Thus, to estimate the systematic uncertainty associated with this procedure, the width of $R_{K\alpha}$ was varied between 0.7 keV and 2.7 keV in steps of 0.2 keV with the center of the region kept at 6.1 keV (see Fig. 19). In Fig. 20, the fitted values for the shift and width were plotted against the width of $R_{K\alpha}$. The average values for the shift and width and their statistical errors for the region 1.3 keV$\leqslant R_{K\alpha} \leqslant$2.1 keV were taken as our final result and the spread of the values was used as the systematic error associated with this procedure. That is,

$$\Delta E_{1s} = \frac{1}{N} \sum_{i=\{1.3,\ldots,2.1\}} \Delta E_{1s}^{(i)}, \tag{5a}$$

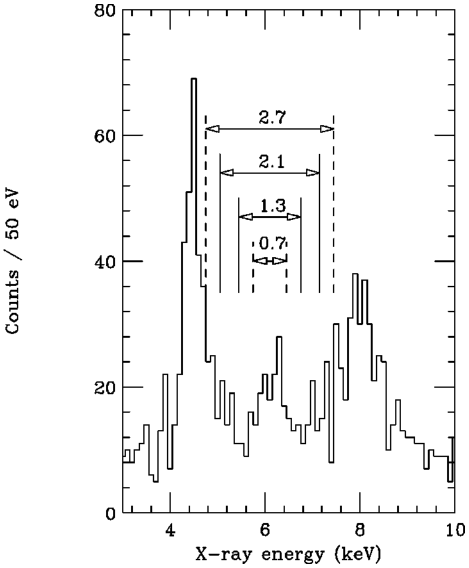

FIG. 19. Different $R_{K\alpha}$ widths plotted on the x-ray spectrum. The average of the values for 1.3 keV$\leqslant R_{K\alpha} \leqslant$2.1 keV were taken to obtain the final results.

$$\sigma_{\text{stat}}(\Delta E_{1s}) = \frac{1}{N} \sum_{i=\{1.3,\ldots,2.1\}} \sigma_{\text{stat}}(\Delta E_{1s}^{(i)}), \tag{5b}$$

and

$$\sigma_{\text{sys}}^{(\text{IF})}(\Delta E_{1s}) = \sqrt{\frac{1}{N-1} \sum_{i=\{1.3,\ldots,2.1\}} (\Delta E_{1s}^{(i)} - \Delta E_{1s})^2}, \tag{5c}$$

and similar expressions for the width and its statistical and systematic errors, where N is the number of $R_{K\alpha}$'s used. Note that, although we call $\sigma_{\text{sys}}^{(\text{IF})}(\Delta E_{1s})$ and $\sigma_{\text{sys}}^{(\text{IF})}(\Gamma_{1s})$ systematic errors for convenience, they are in essence statistical in that they will tend to zero for high statistics.

For the procedure described above, the shift and width obtained were

$$\Delta E_{1s} = -323 \pm 63 \pm 5 \text{ eV}$$

and

$$\Gamma_{1s} = 407 \pm 208 \pm 63 \text{ eV},$$

where the first error is statistical and the second is the systematic error associated with this procedure. The systematic error associated with the energy calibration procedure and the background estimation will be given in Sec. IV A 5. In Fig. 21 and Table III, the results of the fitting for $R_{K\alpha}$ =1.7 keV are shown.

TABLE II. Values of the shift and width for each iteration. The width of $R_{K\alpha}$ was chosen to be 1.7 keV. It is seen that the convergence is quite fast.

No. of iteration	1	2	3	4	5
Shift (eV)	-299 ± 68	-330 ± 62	-384 ± 61	-327 ± 62	-326 ± 62
Width (eV)	595 ± 249	363 ± 194	404 ± 198	394 ± 200	397 ± 200

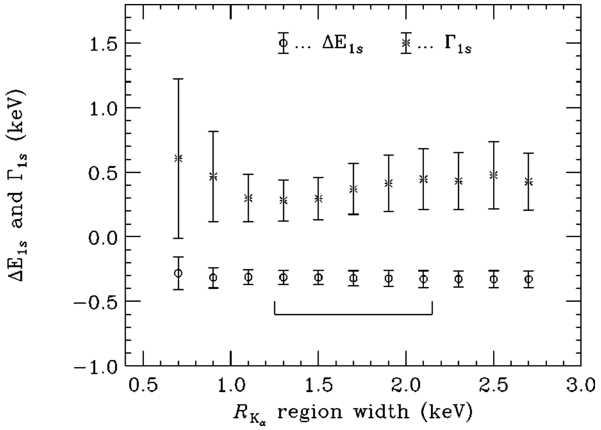

FIG. 20. The shift and width versus the $R_{K\alpha}$ width for the cascade-unconstrained iterative fit.

4. Cascade-constrained iterative fit

The fit to the 3–10 keV region performed as the last step of the iterative fitting procedure in the previous section gave rather unrealistic intensity ratios for the *K*-series lines in K_{complex}, although our criterion for the iterative procedure was that as long as the shape of the left side of the K_{complex} peak is reproduced (without regard to the intensity ratios for the lines in the K_{complex}), the correct values for the shift and width can be obtained.

In order to check the validity of the iterative procedure, it is appropriate to check whether the same result can be obtained when more realistic intensity ratios for the lines in the K_{complex} are used. An iterative fitting procedure was therefore examined with the intensity ratios of the lines in K_{complex} constrained by the cascade code of Borie and Leon [21].

(1) The region $R_{K\alpha}$ was fitted as in the cascade-unconstrained fit described in the preceding section. The free parameters were the shift, the width, and the amplitude of the $K\alpha$ peak.

TABLE III. Results of the cascade-unconstrained iterative fit. The values of the fitting parameters were obtained from the last iteration for $R_{K\alpha}=1.7$ keV. The error values for the intensities of $K\gamma$ and higher lines for the 3–10 keV fit are not shown because they are strongly correlated.

	$K\alpha$ region fit	3–10 keV fit
DOF [a]	31	132
χ^2_{P}	24.446	154.9
χ^2_{P}/DOF	0.789	1.17
ΔE_{1s} (eV)	-326 ± 62	-326 (fixed)
Γ_{1s} (eV)	397 ± 200	397 (fixed)
$K\alpha$ x ray (counts)	113.9 ± 24.7	115.9 ± 17.8
$K\beta$ x ray (counts)	55.2 (fixed)	55.1 ± 28.8
$K\gamma$ x ray (counts)	37.8 (fixed)	37.3
$K\delta$ x ray (counts)	80.4 (fixed)	81.5
$K\epsilon$ x ray (counts)	0.0 (fixed)	0.0
$K\zeta$ x ray (counts)	0.0 (fixed)	0.0
$K\eta$ x ray (counts)	142.2 (fixed)	141.8

[a] Degree of freedom.

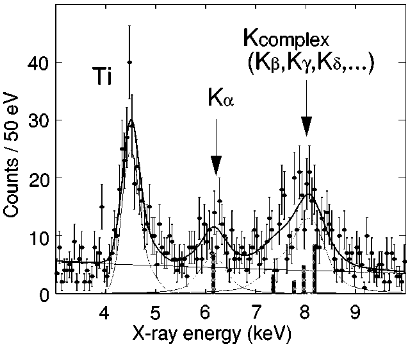

FIG. 21. X-ray spectrum with the fitted curve. This is the result of the last step of the cascade-unconstrained fit for $R_{K\alpha}=1.7$ keV. The bar chart indicates the energy and the relative intensity of each line.

(2) The 3–10 keV region was fitted to the full function keeping the shift and width fixed and varying the amplitude of each line. Here the intensity ratios among the K_{complex} were constrained by the cascade code whose parameters k_{stk} and T were fixed at 1.8 and 1.0 eV and only Γ_{2p} was allowed to vary.

(3) Again the region $R_{K\alpha}$ was fitted, as in the cascade-unconstrained fit described in the preceding section, this time using the full function treating the tail of K_{complex} and the titanium peak as part of the background. The shift, width, and amplitude of the $K\alpha$ peak were free parameters.

(4) The last two steps were repeated until the values of the shift and width converged.

$R_{K\alpha}$ was varied as in the preceding section and the fitted results were evaluated in the same way. The shift and width obtained were

$$\Delta E_{1s}=-323\pm61\pm5 \text{ eV}$$

and

$$\Gamma_{1s}=406\pm206\pm65 \text{ eV},$$

where again the first error is statistical and the second is the systematic error associated with this procedure. These results are fully consistent with those obtained with the cascade-unconstrained iterative fit. The value obtained for Γ_{2p} from the fit was ~0.3 meV, which was within the range of commonly accepted values. Also, the resultant intensity of $K\alpha$, which was not cascade constrained, agreed with the value predicted by the cascade code within 10%.

5. Systematic errors associated with the background estimation and the energy calibration

The systematic error associated with the background estimation was evaluated by varying each coefficient of the quadratic function by one standard deviation, fitting the spectrum by the iterative method with the new background, and observing the change in the fitted results. The background function was expanded around the $K\alpha$ electromagnetic energy so that the changes in the fitted results by the variation of different coefficients are uncorrelated, that is,

$$I_{\text{BG}}(E)=c_0+c_1(E-E^{\text{E.M.}}_{2p\rightarrow1s})+c_2(E-E^{\text{E.M.}}_{2p\rightarrow1s})^2. \quad (6)$$

TABLE IV. Systematic errors associated with background estimation and energy calibration. The systematic errors associated with the iterative fitting procedure are also tabulated.

Parameter	Change in shift (eV)	Change in width (eV)
$R_{K\alpha}$	5	63
c_0	4	36
c_1	3	8
c_2	0	1
Titanium peak position	4	0
Detector resolution	0	7

The change in the fitted result obtained by variation of each coefficient is shown in Table IV, together with the systematic error associated with the iterative fitting procedure. The change in the fitted results due to the variation of different coefficients can be added in quadrature. The systematic error on the fitted result for the background estimation so obtained was

$$\sigma_{\rm sys}^{\rm (BG)}(\Delta E_{1s})=5 \text{ eV}, \quad \sigma_{\rm sys}^{\rm (BG)}(\Gamma_{1s})=37 \text{ eV}.$$

The systematic errors associated with the energy calibration were also estimated. The error associated with the determination of the energy scale was estimated by scaling the statistical error in fitting the titanium peak in Fig. 15 to the energy of the $K\alpha$ peak. The error associated with the determination of the detector resolution was estimated by varying the width obtained by the fit to the titanium peak in Fig. 15 by one standard deviation and observing the change in the $1s$ shift and width. These data are also tabulated in Table IV.

Note again that the ''systematic'' errors associated with the background estimation and the energy calibration are statistical in that they will tend to zero for high statistics.

As seen in Sec. III C 5, there is a slight energy dependence in the x-ray detector energy resolution, although it was ignored. The effect on the final result should be estimated. Since it is rather involved to fully incorporate the energy dependence of the detector resolution in the fitting procedure, the following approximate expression was used in place of Eq. (4) and checked to see if there was any difference in the fitted results:

$$I_K(E) = \sum_{n=2}^{\infty} A_{np\to 1s} \times V(E, E_{np\to 1s}^{\rm E.M.}+\Delta E_{1s}, \Gamma_{1s}, \sigma(E_{np\to 1s}^{\rm E.M.}+\Delta E_{1s})), \quad (7)$$

where $\sigma(E)$ is the energy-dependent detector resolution and the energy dependence estimated in Sec. III C 5 was used. Again the values of $A_{np\to 1s}$ were set to 0 for $n \geqslant 9$.

The differences between the shift and width obtained using Eq. (4) and those obtained with Eq. (7) were 0.1 eV and 4 eV, respectively. These are small compared to other sources of error and thus the energy dependence of the x-ray detector resolution can be safely neglected.

6. Cascade-constrained noniterative fit

To further investigate the robustness of our fitting technique, an independent methodology was tried. In this case, the full spectral region (3–15 keV) was fit. The amplitudes $A_{np\to 1s}$ in Eq. (4) were constrained by the cascade code of Borie and Leon [21]. This assumption imposes a model-dependent bias for which we do not know how to assign a systematic uncertainty. In order to also investigate the sensitivity of the result to the choice of the cascade code parameters, we tried two different cascade parameter sets: (a) $k_{strk}=1.8$, $T=1.0$ eV, and $\Gamma_{2p}=$free and (b) $k_{strk}=$free, $T=$free, and $\Gamma_{2p}=$free.

It should be noted that because this analysis mainly uses $K_{\rm complex}$ to determine the shift and width, these results are nearly statistically independent of the iterative $K\alpha$ fit described above.

The values obtained were $\Delta E_{1s}=-250\pm 44$ eV and $\Gamma_{1s}=584\pm 110$ eV for parameter set (a) and $\Delta E_{1s}=-307 \pm 41$ eV and $\Gamma_{1s}=605\pm 107$ eV for parameter set (b), where the errors quoted are statistical only. The consistency of these results with the iterative fit is evidence that the systematic uncertainties associated with the iterative procedure are correctly estimated.

B. Determination of the $K\alpha$ x-ray yield

In the prompt-time-gate spectrum in Fig. 17, there are 113.9±24.7 kaonic hydrogen $K\alpha$ x rays and 238.4±18.4 titanium K ($K\alpha$ and $K\beta$) x rays. The kaonic hydrogen $K\alpha$ x-ray yield per stopped kaon was estimated by calculating the expected intensity of the titanium K x rays and comparing the titanium K x-ray and kaonic hydrogen $K\alpha$ x-ray intensities in the prompt-time-gate spectrum.

The main contribution to the production of titanium K x rays comes from the incoming kaons exciting titanium atoms when passing through the titanium foil attached to the Teflon degrader. Other sources of titanium K x rays are the two tagged pions from the K^-p reaction, which pass through the titanium foil on the side walls, the beam pions which go through the titanium foil at the front and on the side walls, and low-energy x rays, which can excite titanium by the photoelectric effect.

Since all the kaons stopped in the hydrogen target passed through the titanium foil when entering the target, the same number of kaons contributes to the numbers of the kaonic hydrogen x rays and the titanium x rays in the prompt-time-gate spectrum. Also the number of titanium K x rays due to the two tagged pions is proportional to the number of kaons stopped in the hydrogen, since there is a pair of tagged pions per stopped kaon. For these two contributions, it is possible to estimate the number of titanium x rays generated per stopped kaon and the probability of a generated x ray being detected by the Si(Li) detector. Therefore, when ignoring the contributions from beam pions and low-energy x rays, the kaonic hydrogen $K\alpha$ x-ray yield can be obtained by simply multiplying the estimated number of titanium K x rays per stopped kaon by the ratio of the number of observed x rays and dividing it by the ratio of the detector acceptance to the respective x rays.

As to the contributions from the beam pions and low-energy x rays, they are not directly proportional to the number of stopped kaons. However, it is possible to estimate their contributions to the number of titanium x rays observed in the prompt-time-gate spectrum as we will see below, hence allowing us to subtract these contributions from the total number of observed titanium K x rays before taking the above mentioned ratio.

Therefore the kaonic hydrogen $K\alpha$ x-ray yield per stopped kaon, $Y_{K\alpha}$, is given by the following expression:

$$\begin{aligned} Y_{K\alpha} &= Y_{\mathrm{Ti}} \frac{N_{K\alpha}^{\mathrm{obs}}}{N_{\mathrm{Ti}}^{\mathrm{obs}} - N_{\mathrm{Ti}}^{\mathrm{beam}\ \pi} - N_{\mathrm{Ti}}^{\mathrm{x\ ray}}} \frac{\Omega_{\mathrm{Ti}}}{\Omega_{K\alpha}} \\ &= \frac{N_{K\alpha}^{\mathrm{obs}}}{N_{\mathrm{Ti}}^{\mathrm{obs}} - N_{\mathrm{Ti}}^{\mathrm{bean}\ \pi} - N_{\mathrm{Ti}}^{\mathrm{x\ ray}}} \frac{Y_{\mathrm{Ti}}^{K}\ \Omega_{\mathrm{Ti}}^{K} + Y_{\mathrm{Ti}}^{2\pi}\ \Omega_{\mathrm{Ti}}^{2\pi}}{\Omega_{K\alpha}}, \qquad (8) \end{aligned}$$

where Y stands for the number of x rays produced per stopped kaon, N for the observed or estimated number of x rays in the prompt-time-gate spectrum, and Ω for the detector acceptance for a produced x ray, with an obvious notation for subscripts and superscripts.

The detector acceptance for kaonic hydrogen $K\alpha$ x rays $\Omega_{K\alpha}$, which in this case is simply the solid angle subtended by the detector at the kaon stopping volume since the x-ray absorption in hydrogen is negligible, was estimated to be $2.44 \pm 0.24\,\%$ by a Monte Carlo calculation using the measured kaon stopping distribution. A 10% error was assigned to the estimated value of the solid angle from comparison with the solid angles obtained by changing the kaon stopping distribution to various limiting cases.

In order to estimate Y_{Ti}^{K}, the titanium K x-ray production rate per incoming K^- for kaons that eventually stop in the hydrogen, the velocity distribution of the incoming kaons as they pass through the titanium foil and the titanium K x-ray production cross section for kaon impact as a function of the velocity of the kaon are necessary. The kaon velocity distribution at the titanium foil was obtained from a Monte Carlo calculation. For the K x-ray production cross section, the experimental data for proton impact [22] were simply used, since the cross section is only a function of the projectile velocity [23]. Averaging over the kaon velocity, the average titanium K x-ray production cross section for the kaons passing through the titanium foil was calculated to be 746 ± 100 b, where the error was estimated from the experimental error of Ref. [22]. For a 50-μm-thick titanium foil, this turns out to be $(2.13 \pm 0.29) \times 10^{-1}$ K x rays produced per kaon passing through the foil.

Estimating Ω_{Ti}^{K} requires both the solid angle subtended by the Si(Li) detectors at the points where the titanium x rays are produced and the absorption of the titanium x rays in the titanium foil to be calculated. A Monte Carlo calculation was performed to calculate the distribution of points where the incoming kaons enter the titanium foil. Using this result, and assuming that the points where titanium x rays are produced distribute uniformly in the foil in the beam direction, the probability of a titanium K x ray produced in the titanium foil being detected was calculated (using another Monte Carlo calculation) to be $(3.04 \pm 0.15) \times 10^{-3}$. The error was estimated by changing the distribution of points where titanium x rays are produced to various limiting cases.

The contribution from the two tagged pions was estimated in a similar way to that from the incoming kaons and found to be 5.3% of the contribution from the kaons, that is, $Y_{\mathrm{Ti}}\ \Omega_{\mathrm{Ti}} = Y_{\mathrm{Ti}}^{K}\ \Omega_{\mathrm{Ti}}^{K} + Y_{\mathrm{Ti}}^{2\pi}\ \Omega_{\mathrm{Ti}}^{2\pi} = 1.053 Y_{\mathrm{Ti}}^{K}\ \Omega_{\mathrm{Ti}}^{K}$ in Eq. (8).

The contribution from the low-energy x rays was estimated by assuming that the rate of x rays arriving at the inner surface of the target chamber is uniform over the whole surface and that the x-ray energy spectrum is the same as the prompt-time-gate spectrum. The number of titanium x rays $N_{\mathrm{Ti}}^{\mathrm{x\ ray}}$ in the prompt-time-gate spectrum due to the low-energy x rays exciting the titanium foil was estimated to be 18.1.

The number of titanium x rays due to the beam pions can be obtained using the fact that the numbers of titanium x rays due to the beam pions should be the same in both the prompt-time-gate spectrum and the off-time-gate spectrum, and the number of titanium x rays in the off-time-gate spectrum should be the sum of the number of titanium x rays due to the beam pions and the number created by the low-energy x rays. Therefore, the number of titanium x rays due to the beam pions in the off-time-gate spectrum was estimated by applying the same calculation for the low-energy x-ray contribution to the off-time-gate spectrum and subtracting it from the number of titanium x rays observed in the off-time-gate spectrum. The result obtained was $N_{\mathrm{Ti}}^{\mathrm{beam}\ \pi} = 9.2$.

Putting all these together, the kaonic hydrogen $K\alpha$ x-ray yield per stopped kaon can be estimated to be

$$\begin{aligned} Y_{K\alpha} = & \frac{113.9 \pm 24.7}{\{238.4 - 18.1 - 9.2\} \pm 18.4} \\ & \times \frac{\{(2.13 \pm 0.29) \times 10^{-1}\}\{(3.04 \pm 0.15) \times 10^{-3}\}}{(2.44 \pm 0.24) \times 10^{-2}} \\ & \times 1.053 \\ = & 1.5 \pm 0.5\%. \qquad (9) \end{aligned}$$

The above procedure was also carried out with the spectrum obtained from a smaller fiducial volume to confirm that the observed titanium x rays were not created by kaons stopped in the foil. The result obtained is consistent with the result obtained with the standard fiducial volume.

C. Observation of the L x rays

A peak is also observed in the 1.5–2.1 keV region of the prompt-time-gate spectrum. Some of the detectors were quite noisy in this region; so discriminator threshold level settings ranged from 0.8 to 3 keV. This could potentially produce spurious peaks, but this would be expected to appear in the off-time-gate spectrum and also that in Fig 15, which are quite smooth in this region. For this reason we attribute this peak instead to the kaonic hydrogen L x rays. However, because we are unable to estimate the efficiency of the detector array at this energy, it is not possible to obtain a reliable K/L x-ray yield ratio.

V. RESULTS AND DISCUSSION

Based on our $K\alpha$ iterative fit and combining the various systematic errors in quadrature, the strong interaction shift

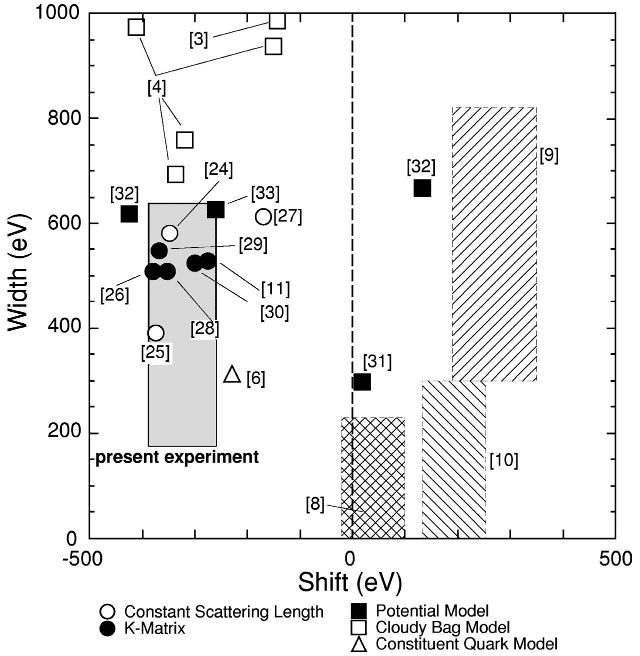

FIG. 22. The shift and width obtained in the present experiment. The one standard deviation region is plotted. The statistical and systematic errors are added in quadrature. Also plotted in comparison are the results of the three previous measurements [8–10], some of the analyses of the low energy $\overline{K}N$ data [11,24–30], and some of the predictions based on a phenomenological potential model [31–33], the cloudy bag model [3,4], and the constituent quark model [6].

and width of the kaonic hydrogen atom $1s$ state were found to be

$$\Delta E_{1s} = -323 \pm 63 \pm 11 \ \text{eV}$$

and

$$\Gamma_{1s} = 407 \pm 208 \pm 100 \ \text{eV},$$

respectively, where the first error is statistical and the second is systematic. Simply applying the Deser-Truman formula [Eq. (1)], the complex $K^- p$ scattering length is

$$a_{K^- p} = (-0.78 \pm 0.15 \pm 0.03) + (0.49 \pm 0.25 \pm 0.12) i \quad \text{fm}.$$

In Fig. 22, the one-standard-deviation regions (the statistical and systematic errors are added in quadrature) of the shift and width are plotted. The results of the three previous measurements [8–10] and some of the analyses of the low-energy $\overline{K}N$ data [11,24–30] are also shown for comparison. Some of the predictions based on a phenomenological potential model [31–33], the cloudy bag model [3,4], and the constituent quark model [6] are also plotted. The sign of our shift is opposite to those obtained in previous experiments and our result is consistent with the analyses of other low-energy $\overline{K}N$ data. This means that the analyses of the low-energy $\overline{K}N$ data (constant scattering length and K matrix) were correct and that there is no anomalous energy dependence of the $\overline{K}N$ amplitude near threshold. There is thus no inconsistency among the low-energy $\overline{K}N$ data and *the long-standing kaonic hydrogen puzzle is resolved.*

As to the kaonic hydrogen $K\alpha$ x-ray yield, the value obtained from this experiment is significantly below 4.38%, the intensity predicted by the cascade code calculation with $\Gamma_{2p} \sim 0.3$ meV (a value obtained from the cascade-constrained iterative fit), $k_{strk} = 1.8$, and $T = 1.0$ eV (values known to reproduce the $\pi^- p$ and $\overline{p}p$ x-ray data fairly well). However, the $K\alpha$ to K_{total} ratio of 0.27 obtained from this experiment is consistent with the cascade code prediction of 0.24 obtained with the parameters given above. If the Γ_{2p} value of the cascade calculation is changed so that the $K\alpha$ x-ray yield is consistent with the experimental value, then the $K\alpha/K_{\text{total}}$ becomes inconsistent with the experimental value. For example, a parameter set of $\Gamma_{2p} = 0.8$ meV, $k_{strk} = 1.8$, and $T = 1.0$ eV gives $Y_{K\alpha} = 1.53\%$ and $K\alpha/K_{\text{total}} = 0.16$

VI. CONCLUSION AND OUTLOOK

In conclusion, kaonic hydrogen atom x rays have been correctly measured for the first time and a distinct $K\alpha$ peak has been resolved. The experimental method, especially the two-pion tagging method, proved to be very effective in improving the signal-to-noise ratio.

The strong interaction shift of the kaonic hydrogen $1s$ state was found to be repulsive. The shift and width were determined to be $\Delta E_{1s} = -323 \pm 63$ (statistical) ± 11 (systematic) eV and $\Gamma_{1s} = 407 \pm 208$ (statistical) ± 100 (systematic) eV, respectively. These results are consistent with the conventional analysis of low-energy $\overline{K}N$ data. This resolves the long-standing kaonic hydrogen puzzle.

The next step for the further understanding of the low-energy $\overline{K}N$ interaction would be precision measurements of both kaonic hydrogen and kaonic deuterium x rays. Kaonic hydrogen x rays provide information on the isospin-averaged $\overline{K}N$ interaction at threshold, whereas kaonic deuterium x rays provide information on a different combination of the $I=0$ and $I=1$ amplitudes at threshold. Thus, combining results of measurements of kaonic hydrogen and deuterium x rays, one can resolve the isospin dependence of the $\overline{K}N$ interaction at threshold.

ACKNOWLEDGMENTS

We wish to acknowledge theoretical discussions with K. Yazaki and M. Arima. We thank T. Harada for the electromagnetic calculation of the kaonic hydrogen atomic states. We also wish to thank the JEOL staff K. Shibuya, H. Ohkubo, T. Watanabe, and especially M. Kuwata for their continuous effort in developing the Si(Li) x-ray detectors. We would like to thank E. Widmann, K. Nagamine, I. Arai, T. Yamazaki, and K. Nakai for their support. We thank E. Klempt and the ASTERIX Collaboration for the use of their cylindrical wire chambers. We are indebted to the KEK staff, especially M. Iwai, R. Ohkubo, K. H. Tanaka, and S. Ishimoto. One of the authors (T.M.I.) is grateful to A. Sanderson for many useful comments and suggestions on the manuscript. This work was supported financially by KEK, with additional contributions from the Grant-in-Aid for International Scientific Research of the Ministry of Education, Science, Sports and Culture, Japan Society for Promotion of Science (Japan), the Natural Science and Engineering Research Council of Canada (Canada), the National Science Foundation, and the Department of Energy (U.S.).

[1] S. Deser, M. L. Goldberger, K. Baumann, and W. Thirring, Phys. Rev. **96**, 774 (1954); T. L. Trueman, Nucl. Phys. **26**, 57 (1961); A. Deloff, Phys. Rev. C **13**, 730 (1976).
[2] E. A. Veit, B. K. Jennings, R. C. Barrett, and A. W. Thomas, Phys. Lett. **137B**, 415 (1984).
[3] E. A. Veit, B. K. Jennings, A. W. Thomas, and R. C. Barrett, Phys. Rev. D **31**, 1033 (1985).
[4] G. He and R. H. Landau, Phys. Rev. C **48**, 3047 (1993).
[5] M. Arima, S. Matsui, and K. Shimizu, Phys. Rev. C **49**, 2831 (1984).
[6] T. Hamaie, M. Arima, and K. Matsui, Nucl. Phys. **A591**, 675 (1995).
[7] R. F. Jaffe and C. L. Korpa, Comments Nucl. Part. Phys. **17**, 163 (1987).
[8] J. D. Davies, G. J. Pyle, G. T. A. Squier, C. J. Batty, S. F. Biagi, S. D. Hoath, P. Sharman, and A. S. Clough, Phys. Lett. **83B**, 55 (1979).
[9] M. Izycki *et al.*, Z. Phys. A **297**, 11 (1980).
[10] P. M. Bird, A. S. Clough, K. R. Parker, G. J. Pyle, G. T. A. Squier, S. Baird, C. J. Batty, A. I. Kilvington, F. M. Russell, and P. Sharman, Nucl. Phys. **A404**, 482 (1983).
[11] A. D. Martin, Nucl. Phys. **B179**, 33 (1981).
[12] M. Iwasaki *et al.*, Phys. Rev. Lett. **78**, 3067 (1997).
[13] S. N. Nakamura *et al.*, Nucl. Instrum. Methods Phys. Res. A **408**, 438 (1998).
[14] JEOL Engineering Co., 3-1-2 Musashino, Akishima, Tokyo 196-0021, Japan.
[15] E. Browne and R. B. Firestone, *Table of Radioactive Isotopes* (John Wiley & Sons, New York, 1986).
[16] T. Harada (private communication).
[17] Particle Data Group, R. M. Barnett *et al.*, Phys. Rev. D **54**, 1 (1996).
[18] S. Baker and R. D. Cousins, Nucl. Instrum. Methods Phys. Res. A **221**, 437 (1984).
[19] C. R. Batty, S. D. Hoath, and B. L. Roberts, Nucl. Instrum. Methods **137**, 179 (1976).
[20] W. Gautschi, SIAM (Soc. Ind. Appl. Math.) J. Numer. Anal. **12**, 635 (1969).
[21] E. Borie and M. Leon, Phys. Rev. A **21**, 1460 (1980).
[22] G. A. Bissinger, J. M. Joyce, E. J. Ludwig, W. S. McEver, and S. M. Shafroth, Phys. Rev. A **1**, 841 (1970).
[23] J. D. Garcia, R. J. Fortner, and T. M. Kavanagh, Rev. Mod. Phys. **45**, 111 (1973).
[24] J. K. Kim, Phys. Rev. Lett. **14**, 29 (1965).
[25] M. Sakitt, T. B. Day, R. G. Glasser, and N. Seeman, Phys. Rev. **139**, 719 (1965).
[26] F. von Hippel and J. K. Kim, Phys. Rev. Lett. **3**, 1303 (1968).
[27] J. Conboy, Rutherford Appleton Laboratory Report No. 91, 1985 (unpublished).
[28] B. R. Martin and M. Sakitt, Phys. Rev. **183**, 1345 (1969).
[29] A. D. Martin and G. G. Ross, Nucl. Phys. **B16**, 479 (1970).
[30] R. H. Dalitz, J. McGinley, C. Belyea, and S. Anthony, in ‘‘Proceedings of the International Conference on Hypernuclear and Kaon Physics,’’ Heidelberg, 1982, edited by B. Poth, Report No. MPIH-1982-V20, p. 201.
[31] K. S. Kumar and Y. Nogami, Phys. Rev. D **21**, 1834 (1980).
[32] K. Tanaka and A. Suzuki, Phys. Rev. C **45**, 2068 (1992).
[33] P. B. Siegel and B. Saghai, Phys. Rev. C **52**, 392 (1995).